Magnetic tunnelling in $Fe\text{-}Al_2O_3\text{-}Fe$ trilayers with radio-frequency sputtered Al_2O_3 barrier layers

1998 J. Phys.: Condens. Matter 10 6629

(http://iopscience.iop.org/0953-8984/10/30/004)

J. Phys.: Condens. Matter **10** (1998) 6629–6642. Printed in the UK PII: S0953-8984(98)90477-5

Magnetic tunnelling in Fe–Al_2O_3–Fe trilayers with radio-frequency sputtered Al_2O_3 barrier layers

Ch Féry†‖, L Hennet†, O Lenoble†, M Piecuch†, E Snoeck‡ and J-F Bobo§

† LPM, URA CNRS 155, UHP, BP 239, 54506 Vandoeuvre-lès-Nancy, Cédex, France
‡ CEMES, CNRS, 29 rue J Marvig, 31055 Toulouse, Cédex, France
§ LPMC, UMR 5830 CNRS-UPS-INSA, INSA, Department Génie Physique, 31077 Toulouse, Cédex 4, France

Received 7 January 1998, in final form 28 April 1998

Abstract. We have prepared iron and Al_2O_3 thin films and Fe–Al_2O_3–Fe trilayers by RF magnetron sputtering. The argon pressure during the process is found to have a significant influence on the microstructure and the coercivity of the Fe layers so that we could obtain Fe–Al_2O_3–Fe trilayers with a spin-valve-like magnetic behaviour for Al_2O_3 thickness as thin as 9 Å. Perpendicular transport measurements of such junctions indicate tunnel behaviour with barrier heights close to 1.5 eV while the barrier width is consistently lower than the nominal Al_2O_3 thickness. Magnetoresistance of these samples reaches up to 1.1% at room temperature.

1. Introduction

The discovery of giant magnetoresistance (GMR) in metallic magnetic multilayers like Fe–Cr [1] or Cu–Co [2–4], spin-valve structures like FeNi–Au–Co trilayers [5] or granular alloys [6, 7] has opened an exciting domain of research with potential applications for magnetic sensors or non volatile data storage. GMR is based on spin dependent scattering, i.e. the difference of mean free path between spin-up and spin-down carriers in a two current model. In fact, another spin dependent effect can lead to strong magnetoresistance: it is spin-polarized tunnelling between two ferromagnets. This effect occurs for junctions made with two ferromagnetic metals separated by an insulating layer. This kind of structure was first studied by Jullière [8] in 1975. In the 70s, MR was only reported at low temperature. This situation has recently been improved with the observation of spin-dependent tunnelling at room temperature [9–12] in metal–insulator–metal trilayers. The most widely used insulating layers are Al_2O_3 films, but several other materials have been tested, like AlN [12], $SrTiO_3$ [13], HfO_2 or MgO [14] which have not shown magnetoresistive effect at room temperature in contrast to Al_2O_3. For example Miyazaki and Tezuka [9] have prepared Fe–Al_2O_3–Fe junctions where aluminum oxide is obtained by air oxidation of metallic Al films. They have observed up to 18% of magnetoresistance at room temperature and for applied fields lower than 50 Oe. The junction resistance they measured was rather low (less than 1 MΩ μm^2), which might suggest that a phenomenon other than tunnelling is

‖ Contact author: Christophe Féry, Department of Materials Science and Engineering, 416 Escondido Mall, Building 550, Stanford University, Stanford, CA 94305-2205, USA. E-mail address: fery@leland.stanford.edu.

0953-8984/98/306629+14$19.50

responsible for the observed MR. But other authors have confirmed MR in tunnel junctions [10, 11, 15]: they used *in situ* plasma oxidation of thin (≈10 to 20 Å) metallic Al films. This technique appears to be a better way than air exposure to obtain tunnelling barriers with junction resistance up to 100 MΩ μm^2 and MR ratios exceeding 15% at room temperature [16]. However, plasma oxidation of a very thin metal film can also lead to over-oxidation, contaminate the ferromagnetic underlayer and therefore reduce its spin polarization. A decrease of the spin polarization of the ferromagnetic layers will induce a decrease of the magnetoresistance. The maximum expected magnetoresistance at low bias, according to Jullière [8], is given by equation (1):

$$\frac{\Delta R}{R_{sat}} = \frac{2P_1P_2}{1 - P_1P_2} \tag{1}$$

where the spin polarizations P_i ($i = 1, 2$) at the Fermi level for both electrodes indexed 1 and 2 are:

$$P = \frac{n^{\uparrow}(E_F) - n^{\downarrow}(E_F)}{r^{\uparrow}(E_F) + n^{\downarrow}(E_F)}. \tag{2}$$

The values of spin polarizations for most ferromagnetic transition metals, measured by spin-dependent tunnelling between a ferromagnet and a superconductor [17] and the expected tunnel magnetoresistance ratios obtained by equation (1) are reported in table 1. Parkin *et al* [11] and Bobo *et al* [18] have already reported that excessive plasma oxidation of 10–20 Å thick Al layers would lead to a decrease or the disappearance of tunnelling magnetoresistance. Bobo *et al* also report the oxygen presence in Co underlayers by XPS depth profiling. Therefore, a different way of obtaining Al_2O_3 barrier layers without the use of plasma oxidation could prevent this over-oxidation effect. We present in this paper spin-polarized tunnelling of Fe–Al_2O_3–Fe trilayers where the Al_2O_3 barrier is directly radio-frequency (RF) sputtered from a ceramic target. This solution has also been tested by Plaskett *et al* [12] who found a non-reproducible tunnelling magnetoresistance.

Table 1. Tunnel magnetoresistance expected at 0 K between two transition metal electrodes; their spin polarizations P, according to [17], are also displayed (all values in %).

	Electrode 1		
Electrode 2	Fe	Co	Ni
Fe ($P = 40 \pm 2\%$)	38	33	20
Co ($P = 35 \pm 3\%$)	33	28	18
Ni ($P = 23 \pm 3\%$)	20	18	11

Another requirement for obtaining tunnelling magnetoresistance is to be able to align the magnetizations of both electrodes either parallel or antiparallel. Several ways can be attempted including hard pinning layers [18], exchange biasing antiferromagnetic layers like MnFe [11], two materials with different coercivities (i.e. CoFe and NiFe) or finally managing to get a coercivity difference due to the morphology/anisotropy of the ferromagnetic layers. This last approach was tested by Miyazaki and Tezuka [9] in the Fe–Al_2O_3–Fe system. While these last authors deposited iron films at two different substrate temperatures, we take advantage of the influence of the argon pressure during sputtering to control the coercivity of our films. Finally, the measurement of the tunnel transport properties of such trilayers requires the fabrication of current-perpendicular-to-planes devices (CPP). The main two techniques currently used are lithography [11, 18] or *in situ* contact masks [10, 11]. The

advantage of lithography is the number of devices available per wafer after fabrication and the size range of the junctions (from submillimetric to submicronic) but it is a longer process. In this study, we used *in situ* submillimetric contact masks, allowing a faster sample fabrication and analysis.

After a brief description of our experimental procedures, we will present a detailed study of the structural and magnetic properties of iron films as a function of the sputtering working pressure. Then, we will present structural, magnetic and transport properties of Fe–Al_2O_3–Fe trilayers.

2. Experimental procedures

Films were deposited onto microelectronics-grade (100) oxidized Si or float-glass substrates maintained at room temperature in an Alcatel SCM 650 automated sputtering apparatus. Typically 99.5% pure Fe and Al_2O_3 targets were mounted on 10 cm diameter RF magnetron cathodes. The base pressure was 7×10^{-7} mb and 99.999% purified argon was introduced into the chamber through a pressure-regulated valve up to an operating pressure adjustable from 2×10^{-3} mb up to 7×10^{-2} mb (limits of stability of the plasma). All films were deposited with a substrate-to-target distance equal to 10 cm and in dynamic mode, i.e. substrates are scanned over the cathodes at 2 r.p.m in order to obtain films with uniform thickness. The sputtering conditions of the iron and Al_2O_3 films are summarized in table 2. Concerning the preparation of the iron films, all the preparation parameters have been fixed, except the argon working pressure P_{Ar}.

Table 2. Preparation condition summary.

Fe	process: RF magnetron (shielded) applied power density: 5 W cm^{-2} working pressure (P_{Ar}): from 2×10^{-3} to 6.7×10^{-2} mbar deposition rate: from 4 Å/scan to 10 Å/scan
Al_2O_3	process: RF magnetron applied power density: 5 W cm^{-2} working pressure (P_{Ar}): 3×10^{-3} mbar deposition rate: ≈4.25 Å/scan

Topological characteristics of the films have been studied by small angles x-ray scattering (SAXS) with a Philips high resolution diffractometer at the Co Kα1 line ($\lambda = 1.788\,92$ Å). A monochromatic parallel beam is obtained by a four-crystals monochromator. These experiments were performed in $\theta/2\theta$ specular mode. Diffractograms like those presented in figure 2 exhibit several Kiessig fringes whose position and intensity are characteristic of the optical index (i.e. the density of the films), their thickness and their roughness. We used the standard recursive model [19] for the SAXS diffractograms simulations. Scanning electron microscopy (SEM) was performed on a Hitachi S 2500 microscope equipped with a LaB_6 filament. The upper detector of the microscope was used to collect secondary electrons, samples being introduced inside the objective lens. Such procedure leads to an optimal lateral resolution close to 25 Å. Finally, the fine structure of the trilayers was studied by high resolution transmission electron microscopy (HRTEM) on cross sectional specimens in order to study the stacking sequence and the interface structure. These experiments were carried out on a Philips CM30/ST microscope working at 300 kV with a point resolution of 1.9 Å. The samples were first cut in two parts, glued face to face then mechanically

polished. The final thinning to electron transparency was achieved by argon-ion milling (5 kV, 5 mA, 15°) at liquid nitrogen temperature to avoid any diffusion and mixing between the layers.

Optical transmission experiments were performed in the range 3200–190 nm at room temperature using a Hitachi U-4001 scanning spectrophotometer. Calibration baselines and a bare float-glass substrate were also measured to extract the optical transmission of the Al_2O_3 layer. Analysis of the transmission spectra was done by fitting to a multiple-reflection optical model [20]. The index of refraction n of both the alumina and the glass substrate were assumed to behave like

$$n = a/\lambda^2 + b \tag{3}$$

where a and b are constants and are determined by the fit. The Al_2O_3 thickness was also a fit parameter. Magnetization curves of single iron films were recorded with a combination of polar and longitudinal magneto-optic Kerr effect (MOKE) apparatus operating with a 6328 Å He–Ne laser. This technique is appropriate for measuring the magnetization curves of our thin films since their thickness is of the same order of magnitude as the penetration depth of the laser (≈ several hundreds of Å). On the other hand, concerning Fe–Al_2O_3–Fe trilayers, we used a standard vibrating sample magnetometer (VSM) to detect the contributions of both top and bottom layers with the same sensitivity (in contrast to MOKE which is essentially surface sensitive). All these magnetization measurements were performed at room temperature on unpatterned Fe–Al_2O_3–Fe trilayers with an area of ≈0.5 cm^2.

For CPP transport measurements, we used *in situ* contact masks made in a 1/10 mm CuBe foil which allow us to prepare 16 junctions on a sample. Their patterning was achieved by a standard chemical etch technique with a path width of 0.20 mm. In the first place, Cr/Au contacts were evaporated onto each 20 × 20 mm^2 float-glass substrate. Then the *in situ* masks were sequentially set close to the substrate. Samples were transferred back to the load lock for each contact mask change. Then the load lock was quickly vented and pumped down so that the air exposure was less than 2 minutes. Electrical resistivity and magnetoresistance were measured with a standard two-probe DC technique in perpendicular geometry. This design was chosen to avoid usual artifacts due to non-homogeneous current-distributions in the junction area. The design of the contact masks, illustrated by a schematic view of one sample, is presented in figure 1.

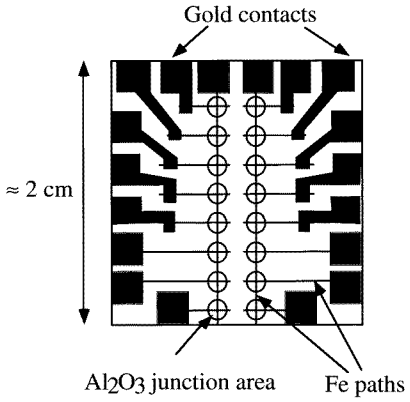

Figure 1. Schematic view of a series of junctions prepared with our contact masks.

3. Results and discussion

SAXS experiments on a series of iron films deposited at various argon working pressures are presented in figure 2. Their simulations, optimized by a logarithmic χ^2 minimization, lead to the determination of their nominal characteristics summarized in table 3. For better fits, we had to include a surface layer and layer thickness local fluctuations to fit the spectra corresponding to the larger roughness (up to 50 Å). One can clearly see that a low pressure process leads to smooth films with a density close to the bulk iron one. In the contrast, for intermediate argon pressures (i.e. from 5×10^{-3} to 3×10^{-2} mb), the roughness of the films reaches larger values and their density is significantly lower than the bulk iron one ($\approx$84% of the bulk density). At last, for the ultimate high argon pressures, films tend to reach the density of bulk iron, despite a larger roughness. The introduction of thickness fluctuations in our model has significantly improved our simulations for intermediate argon pressures which correspond to the rougher case. The quantitative measurements performed by SAXS are confirmed by SEM, as shown in figure 3. Figure 3(a) represents the surface morphology of an iron film deposited at 3×10^{-3} mb where no detail of the surface can be detected within the resolution of the SEM. In contrast, for a film deposited at $1e-2$ mb (see figure 3(b), one clearly observes grains with a lateral size close to 100–200 Å, characteristic

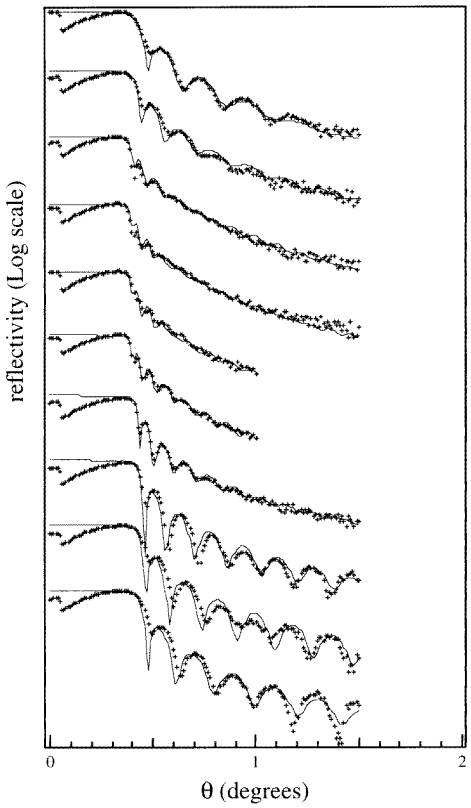

Figure 2. Small angle x-ray reflectometry scans on a series of iron films deposited with the same sputtering conditions except the argon pressure which is indicated in the legend (solid lines are calculated spectra obtained with the model presented in the text).

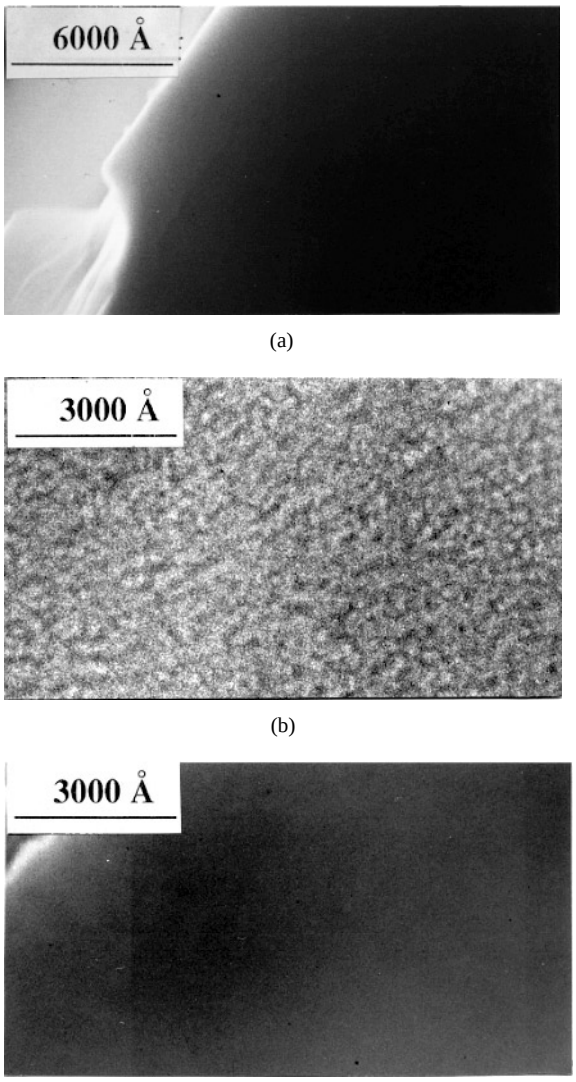

Figure 3. Scanning electron microscope micrographs of three iron films prepared at different argon pressures and exhibiting different surface morphologies: (a) $P_{Ar} = 3 \times 10^{-3}$ mb, (b) $P_{Ar} = 1 \times 10^{-2}$ mb, (c) $P_{Ar} = 7 \times 10^{-2}$ mb.

of a columnar growth. Finally, a film deposited at high argon pressure does not show detectable surface roughness as reported in figure 3(c).

Magnetic hysteresis loops recorded for these iron films are presented in figure 4. The value of the coercive field (H_c) depends on the morphology of the iron films, especially on their density and their roughness. H_c reaches 217 Oe for $P_{Ar} = 2 \times 10^{-2}$ mb while it is as low as 45 Oe for high or low P_{Ar}. Such a result is not surprising, assuming that the rougher iron films are composed of weakly coupled columnar grains. It is well known that in granular systems with sufficiently small grain size (i.e. smaller than the wall width), the magnetization is expected to have a single-domain structure limited by the grain size.

Table 3. Summary of the characteristics of the iron films deduced from SAXS simulations.

P_{Ar} (mb)	Relative density (vs bulk Fe)	Thickness (Å)	Roughness (Å)	Surface layer (Å)	Coercive field (Oe)
2.0×10^{-3}	1.006	227.0	5.0	10.0	43
2.5×10^{-3}	1.002	254.0	5.0	10.0	45
3.0×10^{-3}	1.006	273.0	8.0	8.0	45
5.0×10^{-3}	0.968	350.0	30.0	10.0	84
8.0×10^{-3}	0.875	440.0	30.0	20.0	182
1.0×10^{-2}	0.857	450.0	40.0	30.0	211
2.0×10^{-2}	0.838	452.0	50.0	20.0	217
3.0×10^{-2}	0.838	380.0	40.0	20.0	211
5.0×10^{-2}	0.894	240.0	25.0	30.0	87
6.7×10^{-2}	0.931	95.0	18.0	17.0	43

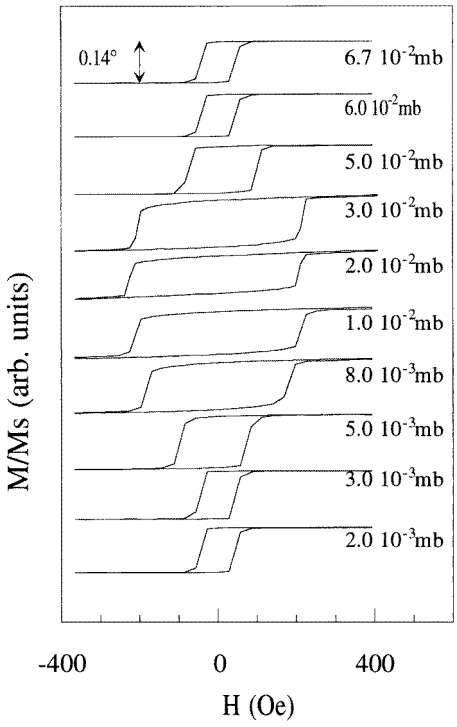

Figure 4. Hysteresis loops measured by Kerr effect on several iron films prepared at various argon pressures.

The most probable mechanism of the magnetization reversal is a coherent rotation of the magnetization within each grain. This mechanism leads to larger coercive fields than in the case of the motion of domain walls and the maximum value predicted for Fe is about 500 Oe [21], therefore twice our experimental result.

Optical transmission spectra confirm the dielectric nature of the Al_2O_3 barrier layers (figure 5). The transmission spectrum of a 2000 Å thick layer is fitted to our model (figure 5) The parameters are displayed in table 4. The alumina index of refraction (n_1) is coherent

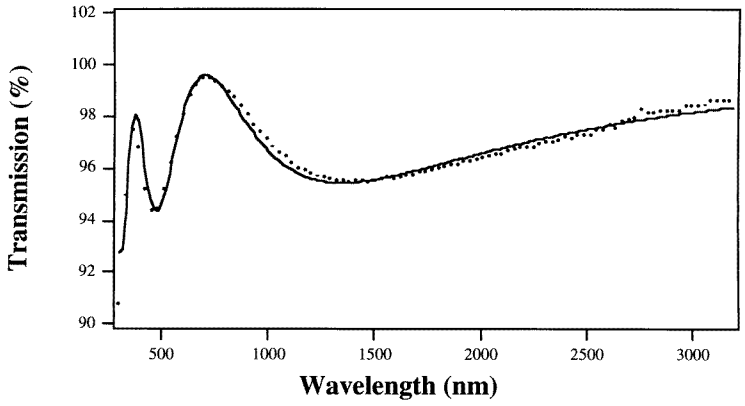

Figure 5. Optical transmission spectrum of a 2000 Å thick alumina layer (solid line = fit, see text).

Table 4. Index of refraction deduced from IR transmission spectra simulations of a 2000 Å Al_2O_3 deposited on a float-glass substrate.

Al_2O_3 thickness	Al_2O_3 index of refraction $n_1 = a_1/\lambda^2 + b_1$		Substrate index of refraction $n_2 = a_2/\lambda^2 + b_2$	
2180 Å	$a_1 = 2.12 \times 10^6$ (Å^2)	$b_1 = 1.54$	$a_2 = 2.3 \times 10^6$ (Å^2)	$b_2 = 1.38$

with the values reported by Ohring [23] (at $\lambda = 5500$ Å we obtain $n_1 = 1.61$, instead of $n_1 = 1.64$ in [22]). The transmission decays below $\lambda \approx 400$ nm because of the absorption onset of float glass. The interband absorption of the sputtered Al_2O_3 film occurs for a shorter wavelength, confirming a band gap larger than 3 eV.

Fe–Al_2O_3–Fe trilayers were prepared with different working pressures P_{Ar} for the two iron films in order to obtain differential coercivities: the first film was deposited at $P_{Ar} = 3.0 \times 10^{-3}$ mb and the second one at $P_{Ar} = 1.0 \times 10^{-2}$ mb. They were separated by an Al_2O_3 barrier with a thickness t_s varying from 0 Å (no barrier) up to several hundred Å. Figures 6(a) and 6(b) are TEM images of two Fe–Al_2O_3–Fe trilayers with different alumina thickness. The low magnification micrograph in figure 6(a) clearly evidences a continuous 64 Å Al_2O_3 barrier in an Fe (200 Å)/Al_2O_3 (64 Å)/Fe (400 Å) trilayer over at least 2 microns. The Fe layers appear both polycrystalline without any preferential orientations. However, the upper Fe layer (deposited at $P_{Ar} = 1.0 \times 10^{-2}$ mb) exhibits a highly disordered and rough columnar structure with a lateral grain size of about a few hundreds of Å, while the bottom Fe layer (deposited at $P_{Ar} = 3.0 \times 10^{-3}$ mb) appears much more regular. The HRTEM experiments performed on a trilayer with thinner alumina layer (figure 6(b), $t_s = 17$ Å) confirm that thin Al_2O_3 barriers remain continuous. In this figure an Fe–Al_2O_3 interface roughness smaller than 5 Å is measured. Figure 7 represents the magnetization curves obtained at room temperature for a series of Fe (200 Å)/Al_2O_3 (t_s)/Fe (400 Å) trilayers with t_s ranging from 0 Å (no alumina deposited) up to 64 Å. It is clear that the two subcycles of the top and bottom iron layers are more and more separated with increasing t_s. For vanishing t_s, the coercive field tends to be uniform and equal to the smallest one (≈50–70 Oe). It is easy to interpret this in terms of direct contact between the two iron layers: once the softer layer magnetization M_1 reverts, all the magnetizations of the grains of the other layer are

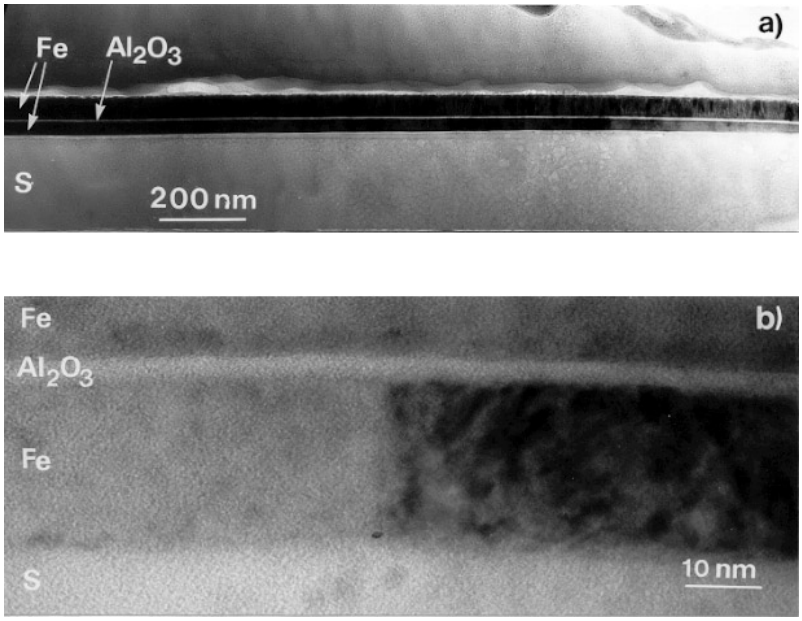

Figure 6. (a) Low magnification micrograph ($\times 88 \times 10^3$) of an Fe (200 Å)/Al_2O_3 (64 Å)/Fe (400 Å) trilayer revealing the continuity of the Al_2O_3 barrier over a long distance. (b) High magnification micrograph ($\times 1.400 \times 10^3$) of an Fe (200 Å)/Al_2O_3 (17 Å)/Fe (400 Å) trilayer evidencing the flatness of the Fe–Al_2O_3 interfaces.

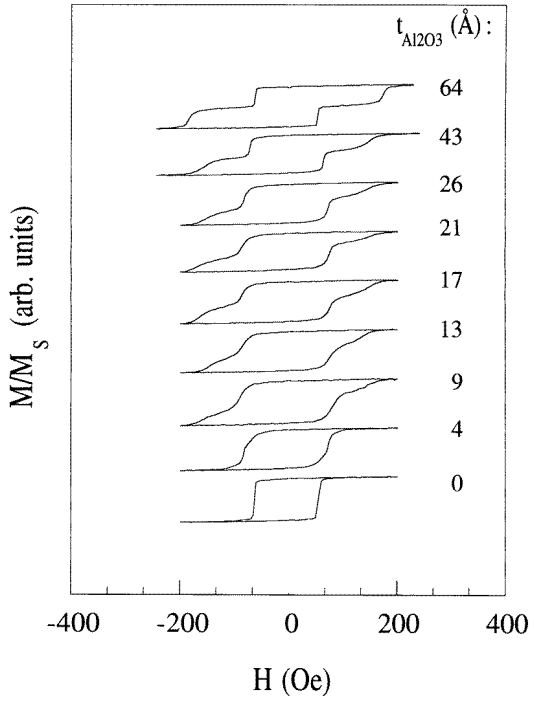

Figure 7. $M(H)$ loops of Fe–Al_2O_3–Fe trilayers recorded at room temperature with a VSM apparatus. The alumina thickness ranges from 0 Å (no alumina) up to 64 Å.

rotated in the same way and M_2 remains parallel to M_1. Above $t_s \approx 9$ Å, the two subcycles are clearly separated; in the field interval $H_{c1} < H < H_{c2}$, a plateau can be distinguished. In this domain, antiparallel configurations of the magnetizations M_1 and M_2 are achieved and this is proof for the uncoupling of the two iron layers. However, one can see that for the smallest alumina thickness (from 43 Å to 9 Å) the cycles are more complex: the soft layer has a relatively well defined coercive field while the hard one seems to saturate progressively. This ferromagnetic coupling of the two Fe layers is either due to direct exchange through pinholes or to dipolar orange peel coupling induced by the roughness of the Fe layers [22].

For $t_S < 70$ Å, our junctions have relatively low resistances and linear ohmic $I(V)$ characteristics, indicative of the absence of tunnelling. However, samples with alumina thickness above 70 Å exhibit linear $I(V)$ curves at low voltages ($V < 10$ mV) and non-linear above (figure 8). Mean barrier heights ($\langle\phi\rangle$) and width ($\langle d\rangle$) are obtained by using Simmons' tunnelling equation [24] for trapezoidal barriers and within the intermediate voltage range (i.e. $V < \phi/e$):

$$I = \frac{A \times 6.02 \times 10^{10}}{d^2}\{\langle\phi\rangle \exp(-1.02d\sqrt{\langle\phi\rangle}) - (\langle\phi\rangle + V) \exp(-1.02d\sqrt{\langle\phi\rangle_V})\} \tag{4}$$

where A is the junction area and $\langle\phi\rangle = (\phi_1 + \phi_2 - |e|V)/2$ is the mean barrier height.

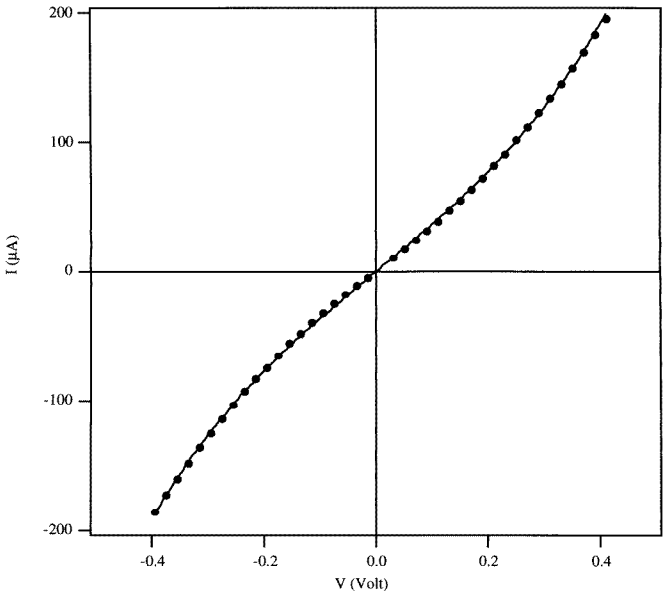

Figure 8. $I(V)$ curve measured for a Fe–Al_2O_3 (89 Å)–Fe trilayer fitted to the Simmons theory of tunnelling ($T = 300$ K).

The mean barrier height is corrected by both barrier profile asymmetry (ϕ_1 and ϕ_2) and voltage dependence (V). The mean barrier heights we deduced are lower than those observed elsewhere [10, 11] but in the same range ($\langle\phi\rangle \approx 1.5$ eV versus $\approx$3 eV). But the barrier widths obtained from fitting are consistently far below the nominal alumina thickness (see figure 8). Such a discrepancy could be explained by interfaces roughness and/or defects in the insulating layer. Samples exhibiting tunnelling-like $I(V)$ curves at room temperature were investigated from 300 K down to 77 K. According to Stratton's theory on tunnelling

temperature dependence [25], the tunnel current is expected to be proportional to the square of the temperature for a constant applied voltage:

$$I(T, V) = I(0, V)[1 + \tfrac{1}{6}(\pi c k_B T)^2] = I(0, V)[1 + AT^2] \tag{5}$$

where c is independent of the temperature and k_B is the Boltzmann constant. Figure 9 shows the $I(T)$ curve for a sample which exhibits tunnelling-like $I(V)$ curves. This $I(T)$ curve has a parabolic shape which could indicate a tunnel behaviour. By using the same method as Simmons to handle the transmission probability it is possible to approximate c as [24]:

$$c = 2\pi \frac{(2m_e)^{1/2} d}{h\phi^{1/2}}. \tag{6}$$

where h is the Planck constant and m_e the electron mass. Basically, tunnel current thermal dependence is very low and would induce a T^2 prefactor $A \approx 3$ to 4×10^{-8}. The thermal change of the junction current with temperature is significantly larger than the one expected by a pure tunnelling process. So we assume there is another origin to the thermal dependence of the $I(T)$ than tunnelling: activated barrier hopping occurs and it can be simply described as:

$$I_{act}(T) = I(0) \exp\left[-\frac{T_0}{T}\right]. \tag{7}$$

We have fitted the $I(T)$ curve displayed in figure 9 with a combination of equations (5) and (7). The contribution of activated hopping clearly dominates above $T \approx 150$ K, with an activation temperature of ≈750 K. This could correspond to a mean energy of 65 meV for impurity levels within the barrier, therefore lower than the barrier height deduced from the $I(V)$ characteristics measured at room temperature. This anomalous behaviour of the $I(T)$ characteristics has already been reported by Miyazaki and Tezuka [26] who assume it is due

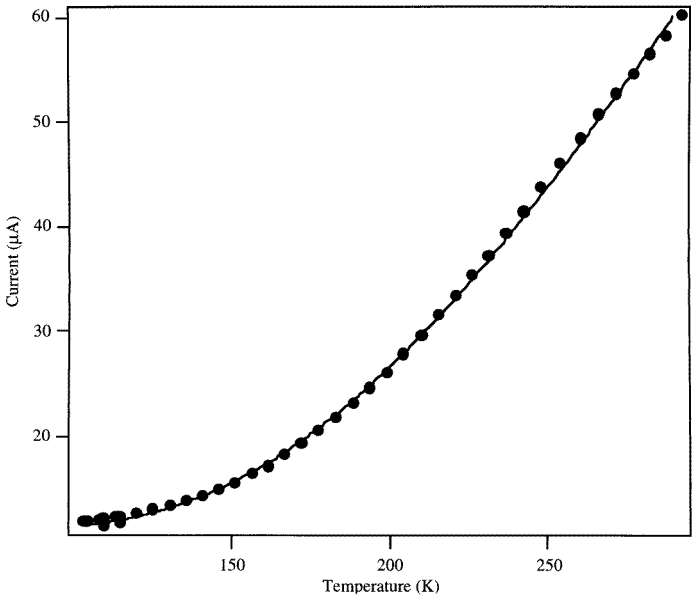

Figure 9. $I(T)$ curve obtained at $V = 0.11$ V for an Fe–Al_2O_3 (89 Å)–Fe junction.

to non-uniform barrier height and width caused by thickness or stoichiometry fluctuations of the AlO_x film.

The variation of the current intensity at low voltage with the applied magnetic field was also investigated. Only room temperature data are presented here; low temperature data are not available. Some junctions exhibit an increase of the ratio V/I when H reaches the soft magnetic layer coercive field and then decreases above the hard magnetic layer coercive field (see figure 10). This junction resistance increase occurs when the system switches from a parallel magnetic configuration to an antiparallel one. The plateau remains for any orientation of the applied magnetic field with respect to the sample, confirming thus that the effect we have measured is not due to spurious planar galvanomagnetic effects. However the magnitude of the magnetoresistance does not exceed 1% at room temperature and the reproducibility yield is very low: typically, less than one tunnelling device in ten displayed magnetoresistance. The maximum amount of magnetoresistance we observed is significantly lower than the expected value which is 38% at low temperature (see table 1 and equation (1)). We might explain this lower observed spin-polarization by the oxidation of the bottom iron electrode when the sample is exposed to air for the contact mask switching. The oxide would cause a spin-flip and therefore a depolarization of the tunnelling current. Another reason for the lower magnetoresistance could be the nature of RF-sputtered alumina since Plaskett *et al* [12] reported larger magnetoresistance and reproducibility with oxidized aluminum and junctions exposed to air during the process. So it is reasonable to conjecture that trouble obtaining magnetoresistance with junctions prepared with sputtered alumina is due to the highly disordered structure of RF-sputtered alumina. If the dielectric barrier contains too many defects like oxygen vacancies, it might have localized states within its forbidden band which would induce a decrease of the mean barrier height and a depolarization of the tunnelling current. The presence of such localized states in the barrier is compatible with the thermal dependence of the junction current as shown in the $I(T)$ dependence. The roughness of the barrier, that we estimate to be close to 3–5 Å, can also play a dominant

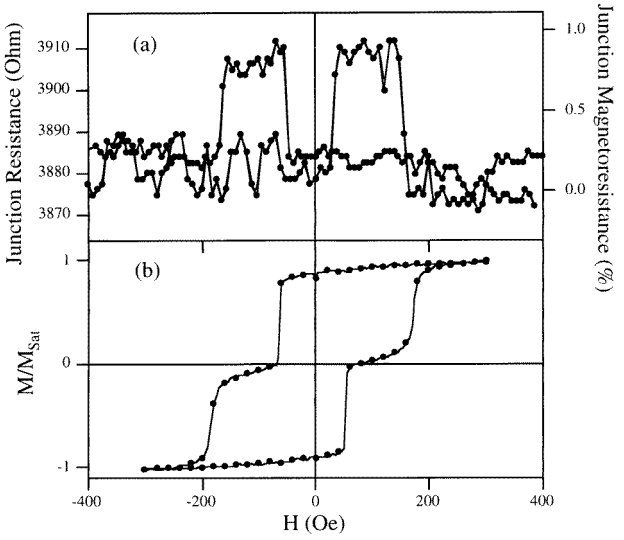

Figure 10. Room temperature magnetoresistance curve measured for an Fe (250 Å)–Al_2O_3 (89 Å)–Fe (400 Å) junction (a) and compared with a magnetization curve on a similar sample (b).

role in the tunnel characteristics: according to Bardou [27], small fluctuations of the barrier thickness induce large tunnel current spatial fluctuations over the junction area and can cause a drastic change of the apparent junction characteristics (effective area, barrier height and width).

4. Conclusion

We have shown in this paper the possibility of preparing iron films at room temperature with various morphologies and coercivities by varying the argon pressure during sputter deposition. This method is very fast and efficient compared to deposition at various substrate temperatures. Fe–Al_2O_3–Fe trilayers with iron layers prepared at low and moderate argon pressures exhibit double coercivities for Al_2O_3 barriers as thin as 9 Å. This result is indicative of the quality of sputtered amorphous alumina ultrathin films for making metal–insulator–metal structures. Optical transmission of RF-sputtered alumina films confirms their dielectric behaviour with a bandgap of at least 3 eV. The transport properties of such trilayers, with an electrode geometry designed for perpendicular measurements, evidences current tunnelling through the alumina barrier. Fitting of the tunnelling $I(V)$ characteristics yields a barrier height of $\approx$1.5 eV and a barrier width which is lower than the nominal Al_2O_3 thickness. We assume the origin of this discrepancy to be either the roughness or the presence of defects in the alumina films. Finally, magnetoresistance ratios of Fe–Al_2O_3–Fe tunnel junctions show a magnetoresistance ratio up to 1.1% at room temperature. This magnetoresistance is lower than the one expected by a simple model ($\approx$38% at 0 K). This is either due to defects in the Al_2O_3 barrier layer or to some contamination of the Fe underelectrode during the preparation process.

Acknowledgments

Support for this work from CNRS and NATO under CRG 971645 is acknowledged.

References

[1] Baibich M N, Broto J M, Fert A, Nguyen Van Dau F and Petroff P 1988 *Phys. Rev. Lett.* **61** 2472
[2] Mosca D H, Petroff F, Fert A, Schoeder P A, Pratt W P Jr and Laloee R 1991 *J. Magn. Magn. Mater.* **94** L1
[3] Parkin S S P, Li Z G and Smith D J 1991 *Appl. Phys. Lett.* **58** 2710
[4] Bobo J F, Baylac B, Hennet L, Lenoble O, Piecuch M, Raquet B and Ousset J C 1993 *J. Magn. Magn. Mater.* **121** 291
[5] Dieny B, Speriosu V S, Parkin S S P, Gouney B A, Wilhoit D R and Mauri D 1991 *Phys. Rev.* B **43** 1297
[6] Berkowitz A E, Mitchell J R, Carey M J, Young A P, Shang S, Spada F E, Parker F T, Hutton A and Thomas G 1992 *Phys. Rev. Lett.* **68** 3745
[7] Xiao J Q, Jiang J S and Chien C L 1992 *Phys. Rev. Lett.* **68** 3749
[8] Jullière M 1975 *Phys. Lett.* **5A** 225
[9] Miyazaki T and Tezuka N 1995 *J. Magn. Magn. Mater.* **139** L231
[10] Moodera J S, Kinder L R, Wong T M and Meservey R 1995 *Phys. Rev. Lett.* **74** 3273
[11] Parkin S S P, Fontana R E and Marley A C 1997 *J. Appl. Phys.* **81** 5521 (abstract)
Gallagher W J, Parkin S S P, Lu Y, Bian X P, Marley A, Roche K P, Altman R A, Rishton S A, Jahnes C, Shaw T M and Xiao G 1997 *J. Appl. Phys.* **81** 3741
[12] Plaskett T S, Freitas P P, Sun J J, Sousa R C, da Silva F F, Galvao T T P, Pinho N M, Cardoso S and Soares J C 1997 *Mater. Res. Soc. Symp. Proc.* **475** 469
[13] Li X W, Lu Y, Gong G Q, Xiao G, Gupta A, Lecoeur P, Sun J Z, Wang Y Y and Dravid P 1997 *J. Appl. Phys.* **81** 5509
[14] Platt C L, Dieny B and Berkovitz A E 1996 *Appl. Phys. Lett.* **69** 2291
Platt C L, Dieny B and Berkovitz A E 1997 *J. Appl. Phys.* **81** 5523

[15] Moodera J S, Kinder L R, Nowak J, LeClair P and Meservey R 1996 *Appl. Phys. Lett.* **69** 708
[16] Moodera J S, Gallagher E F, Robinson K and Nowak J 1997 *Appl. Phys. Lett.* **70** 3050
[17] Meservey R and Tedrow P M 1994 *Phys. Rep.* **238** 173
[18] Bobo J F, Mancoff F B, Bessho K, Sharma M, Sin K, Guarisco D, Wang S X and Clemens B M 1998 *J. Appl. Phys.* **83** 6685
[19] Piecuch M and Nevot L 1990 *Mater. Sci. Forum* **59/60** 93
[20] Heavens O S 1995 *Optical Properties of Thin Solid Films* (New York: Dover)
[21] Kittel Ch 1986 *Introduction to Solid State Physics* 6th edn (New York: Wiley) p 456
[22] Néel L 1962 *C. R. Acad. Sci., Paris* **255** 1676
[23] Ohring M 1992 *The Materials Science of Thin Films* (New York: Academic) p 519
[24] Simmons J G 1963 *J. Appl. Phys.* **34** 2581
[25] Stratton R 1962 *J. Phys. Chem. Solids* **23** 1177
[26] Miyazaki T and Tezuka N 1995 *J. Magn. Magn. Mater.* **151** 403
[27] Bardou F 1997 *Europhys. Lett.* **39** 239